

Article

Advancements on Basic Working Principles of Photo-Driven Oxidative Degradation of Organic Substrates over Pristine and Noble Metal-Modified TiO₂. Model Case of Phenol Photo Oxidation

Alexandra Sandulescu¹, Crina Anastasescu¹, Florica Papa¹ , Monica Raciulete¹ , Anca Vasile¹, Tanta Spataru¹, Monica Scarisoreanu², Claudiu Fleaca², Cristian N. Mihailescu², Valentin S. Teodorescu³, Nicolae Spataru^{1,*}, Maria Zaharescu¹  and Ioan Balint^{1,*}

¹ “Ilie Murgulescu” Institute of Physical Chemistry of the Romanian Academy, Spl. Independentei 202, 060021 Bucharest, Romania; asandulescu@icf.ro (A.S.); canastasescu@icf.ro (C.A.); frusu@icf.ro (F.P.); mpavel@icf.ro (M.R.); avasile@icf.ro (A.V.); tspataru@icf.ro (T.S.); mzaharescu@icf.ro (M.Z.)

² National Institute for Lasers, Plasma and Radiation Physics, Atomistilor Str., No. 409, 077125 Bucharest-Magurele, Romania; monica.scarisoreanu@infpr.ro (M.S.); claudiu.fleaca@infpr.ro (C.F.); cristi.mihailescu@infpr.ro (C.N.M.)

³ Valentin Teodorescu, National Institute of Materials Physics, 405A Atomistilor Street, 077125 Bucharest-Magurele, Romania; teoval@infim.ro

* Correspondence: nspataru@icf.ro (N.S.); ibalint@icf.ro (I.B.)



Citation: Sandulescu, A.; Anastasescu, C.; Papa, F.; Raciulete, M.; Vasile, A.; Spataru, T.; Scarisoreanu, M.; Fleaca, C.; Mihailescu, C.N.; Teodorescu, V.S.; et al. Advancements on Basic Working Principles of Photo-Driven Oxidative Degradation of Organic Substrates over Pristine and Noble Metal-Modified TiO₂. Model Case of Phenol Photo Oxidation. *Catalysts* **2021**, *11*, 487. <https://doi.org/10.3390/catal11040487>

Academic Editor: Ewa Kowalska

Received: 16 March 2021

Accepted: 7 April 2021

Published: 10 April 2021

Publisher's Note: MDPI stays neutral with regard to jurisdictional claims in published maps and institutional affiliations.



Copyright: © 2021 by the authors. Licensee MDPI, Basel, Switzerland. This article is an open access article distributed under the terms and conditions of the Creative Commons Attribution (CC BY) license (<https://creativecommons.org/licenses/by/4.0/>).

Abstract: The specific roles played by both support and noble metals in light absorption, charge separation, and the formation of ·OH and O₂[−] (ROS) are analyzed for light-triggered oxidation of phenol (Ph) over pristine and over noble metal (Ag, Au, Pt) -loaded TiO₂. Experiments show that the supported noble metals act as a light visible absorber, assist the separation of photo-charges and reduction of O₂ to O₂[−]. The O₂[−] oxidizes mildly Ph to oxygenated products (hydroquinone, benzoquinone, and 1,2-dihydroxibenzene). In a parallel process, ·OH radicals, yielded by TiO₂, mineralize Ph to CO₂ by fast reaction sequences. Radical quenching and photo electrochemical measurements (surface photovoltage) confirm independently that the production of ·OH and O₂[−] scale with oxidative conversion of Ph. The selectivity to CO₂ and mild oxidation products is the result of the interplay between catalyst activity for ·OH and for O₂[−] production.

Keywords: photocatalytic mild oxidation; photocatalytic mineralization; phenol oxidation; TiO₂ modified with noble metals; surface photovoltage; O₂ photo reduction; reactive oxygen species; charge recombination

1. Introduction

The sun light driven photo oxidation processes of organic matter are of great importance for several practical reasons: (i) imply low material and operational costs, (ii) are potentially able to clean water and air by mineralization of organic pollutants to CO₂ [1–4], and (iii) are attractive alternative routes for selective synthesis of high-added value oxygenated products [5–7].

The thermodynamic of organics oxidation is downhill process ($\Delta G < 0$), the light being used to speed up chemical reaction via generation of charge carriers. The general accepted steps in photocatalytic processes are: (i) light absorption by photocatalysts followed by generation of e[−] and h⁺ charges; (ii) charge transfer to reactant substrate intermediated by reactive oxygen species, ROS; (iii) development of redox processes with participation of e[−], h⁺, and ROS on surface and vicinity of photocatalysts. Metals are involved actively in all essential reaction steps, determining the final overall photocatalytic efficiency [8,9].

The prevalent reaction mechanism in liquid phase depends on a series of factors including nature of photocatalyst, reaction media, and reacting organic substrate. The reac-

tion mechanism, described well by the Langmuir–Hinshelwood adsorption equation [10], implies the interaction of photogenerated charges with the adsorbed species, at a time scale of 10^{-10} to 10^{-5} s [11]. The photo generated charges (e^- and h^+) react first with hydroxyl groups of adsorbed H_2O and O_2 to yield reactive $\cdot OH$ ($H_2O + h^+ \rightarrow \cdot OH + H^+$) and $\cdot O_2^-$ ($O_2 + e^- \rightarrow O_2^-$) ROS [9]. The oxidative conversion of organic compounds is intermediated by formation and diffusion of ROS to reaction scene [12], which can be remote from the illuminated surface [13].

Metals dispersed on surface of active materials (i) help separation of photo generated charges, (ii) work as cocatalyst by mediating the charge transfer to reacting substrates, (iii) favor the formation of O_2^- , (iv) control the selectivity of oxidation process, (v) bend the energy bands of photocatalysts at solid-liquid interfaces, (vi) modify the light absorbing property of materials, (vii) contribute to enhancement of photocharge production in visible wavelength domain by surface plasmon resonance (SPR) phenomenon [9]. The Schottky regions built at metal-oxide interfaces contribute to electron and hole separation, leading to increased efficiency of photo-driven redox processes. The charge separation efficiency is validated experimentally by the comparing the PL (Photoluminescence) emission intensity of metal-loaded photocatalysts with pristine oxide [14,15]. The bending of valence band (VB) and conduction band (CB) depends on nature of metal and pH of solution. Metals shift the light absorption edge, in many cases with beneficial effects on efficiency. Noble metals exhibit visible light absorption peaks due SPR phenomenon, which is a collective electron oscillation in metal nanoparticles induced by visible light absorption. The SPR was reported to have in some cases favorable effects on photo-driven redox processes performed in visible light [16–18].

In spite of a large number of published researches, essential issues in photocatalysis remain to be elucidated. For example, the specific contribution of metal and support to formation of O_2^- and $\cdot OH$ is, in many cases, controversial, although it is of crucial importance. The predominance of one reaction pathway over the other affects the selectivity of photocatalytic oxidation reaction. The reaction of an organic matter with $\cdot OH$ is unselective, yielding CO_2 , whereas oxidation pathway with $\cdot O_2^-$ on surface of solid or on its premises proceed apparently with high selectivity to oxygenated products.

The general aim of this research is to gain a deeper insight on particularities showed by metal-modified oxide photocatalysts compared to pristine semiconductor oxides in what concerns ROS generation, charge separation, reaction mechanism of organic compounds oxidative conversion. The role of active participants in the oxidative degradation pathways are analyzed in detail. The light-driven (sun or visible light) oxidation of phenol over pristine and metal (Ag, Au, Pt)-modified TiO_2 was chosen as model reaction. To uncover the complex reaction network associated to photo-driven oxidation of organic compounds, we analyzed comparatively: (i) the relative efficiency of supported noble metals in separation of photo charges and implicitly the impact on photocatalytic activity, (ii) the specific contribution of metal and of oxide support to ROS ($\cdot OH$ and O_2^-) formation, (iii) the relationship between O_2^- formation and reaction selectivity to oxygenated products, (iv) the correlation between the activity of catalyst for mineralization of organic substrate to CO_2 and the amount of $\cdot OH$ generated under light irradiation, and (v) the relationship between nature of supported metals and surface photovoltage (SPV) generated under light irradiation in connection with material capacity to generate O_2^- , with obvious implications in reaction mechanism.

2. Results and Discussion

2.1. Characterization Data

The TEM (Transmission Electron Microscopy) analysis of noble metals dispersed on TiO_2 prepared by laser pyrolysis shows well dispersed Pt on TiO_2 support (Figure 1A). The Ag and Au particles are significantly larger than of Pt (see TEM images in Figure 1B,C). Individual spherical Au nanoparticle of around 5 nm can be observed in Figure 1C.

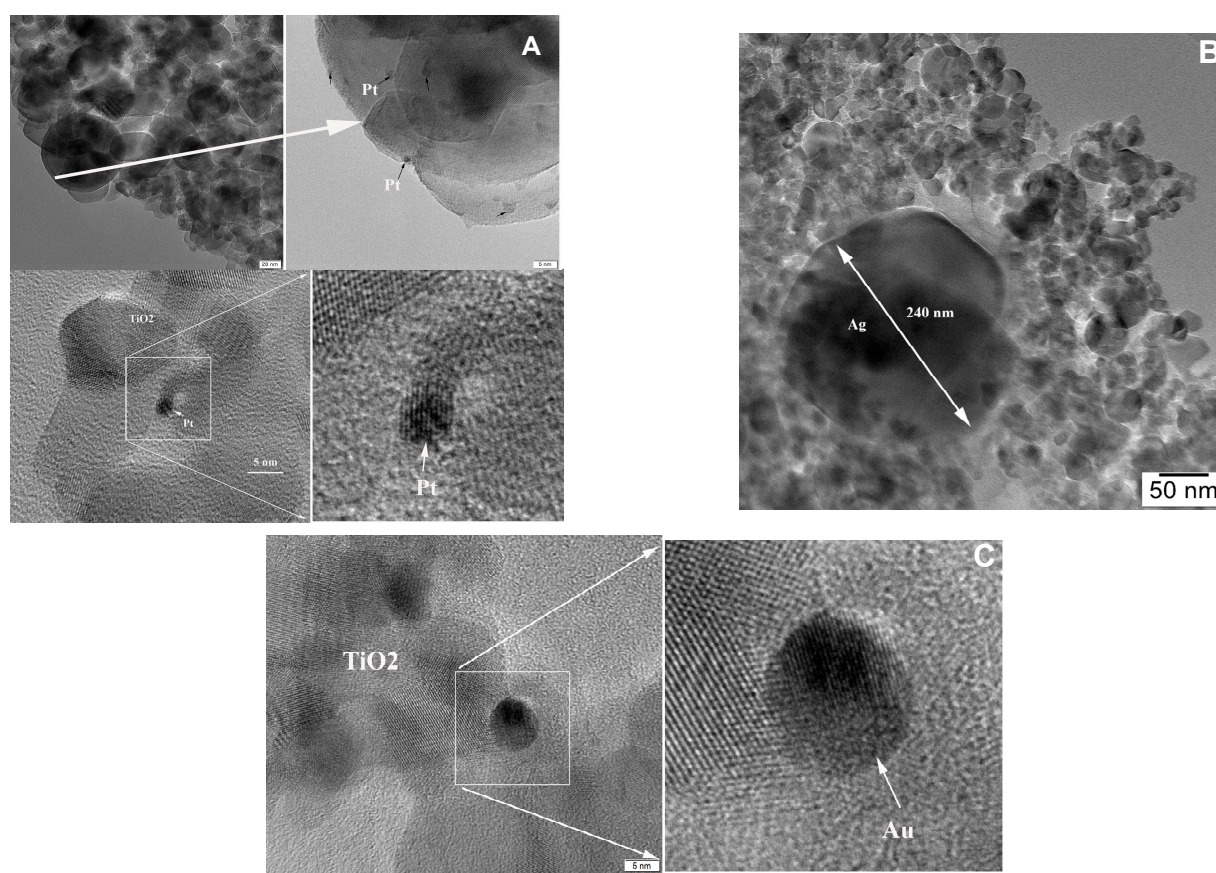


Figure 1. Suggestive TEM images of metal-loaded TiO₂ samples: Pt/TiO₂ (A), Ag/TiO₂ (B) and Au/TiO₂ (C).

The most relevant characterization data obtained by various experimental methods are presented comparatively in Table 1. More details are given in Supplementary Information.

Table 1. Comparative characterization data of investigated materials collected from EDAX (Energy Dispersive X-ray Analysis), XPS (X-ray Photoelectron Spectroscopy), and TEM measurements.

Samples	Cryst. Size/nm ^a	Metal Content/at.% (wt%)		Metal Particle Size/nm		Ti ³⁺ /at. % ^f	Oxid. State ^g
		EDAX ^b	XPS ^c	TEM ^d	Chem. ^e		
TiO ₂	18.8	-	-	-	-	0	-
Ag/TiO ₂	19.3	0.04 (2.7)	0.04 (2.7)	>50	-	22.9	Ag ⁰
Au/TiO ₂	19.8	0.01 (2.5)	0.02 (5.0)	6	-	10.9	Au ⁰
Pt/TiO ₂	20.6	0.01 (2.4)	0.002 (4.8)	2	1	8.8	Pt ⁰

^a—TiO₂ crystallite size determined by Scherrer method from XRD diffractograms; ^b—metal loading evaluated by EDAX; ^c—metal content estimated from XPS data; ^d—metal particle size determined from TEM micrographs; ^e—metal particle size determined by CO chemisorption measurements; ^f—atom percentage of Ti³⁺ in TiO₂ matrix derived from XPS measurements; ^g—metal oxidation state analysis performed XPS measurements.

The XPS analysis revealed that the supported noble metals on TiO₂ were in metallic state (see the XPS data presented in Supplementary Information). Titanium in TiO₂ was in the form of Ti⁴⁺ whereas the metal-loaded TiO₂ contained variable amounts of Ti³⁺ (see Table 1 and Supplementary Information).

The average size of Pt particles supported on TiO₂ estimated from CO chemisorption measurements is ≈1 nm, corresponding to metal dispersion of around 40%. This result is in fair agreement with TEM result evidencing supported Pt nanoparticles of 1–2 nm (see Figure 1A).

The light absorption features of all investigated materials exhibit the characteristic band edge energies of TiO₂ at ≈400 nm (see Figure 2). The plots of Kubeka–Munk function

(F(R)) in Figure 2 describe light absorbance of solid samples. The SPR maxima of Ag and Au nanoparticles are clearly visible at 460 and 544 nm, respectively. Assuming the indirect allowed transitions, the optical band gaps of all investigated materials, obtained by extrapolation of linear part of $([F(R)] hv)^{1/2}$ versus hv plots, are around 3.1 eV (see the inset of Figure 2). The close values of optical band gaps, makes difficult to predict the order of photocatalytic activity, based only on light absorption data.

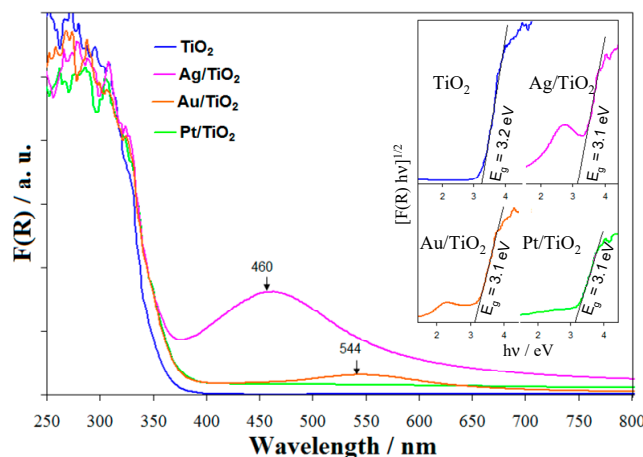


Figure 2. Comparative F(R) spectra and indirect optical band gap derived from Tauc representation (inset) for investigated photocatalysts.

2.2. Photocatalytic Test Results

The experimental data concerning reactant and product distribution, carbon balance, and conversion of phenol (Ph) over bare and metal-modified TiO₂ in aqueous media after 6 h of reaction time are presented in Table 2.

Table 2. Phenol conversion to gaseous and liquid products and carbon balance measured after 6 h of reaction time.

Photocatalysts	C Inlet ^a		C Outlet ^a					
	Ph/ μ moles	Ph/ μ moles	CO ₂ / μ moles	HQ/ μ moles	BQ/ μ moles	1, 2 DHBz/ μ moles	Carbon Balance/%	Phenol Conversion/% ^b
TiO ₂	362.9	331.5	15.6	0	0	0	95.6	8.7
Ag/TiO ₂	369.8	324.5	6.5	7.9	0	1.3	92.0	12.2
Au/TiO ₂	356.2	324.6	13.8	11.1	0	0	98.1	8.9
Pt/TiO ₂	367.9	309.7	21.6	13.3	0.4	1.5	94.2	15.8

^a— μ moles of carbon contained by inlet phenol, non-reacted outlet phenol (Ph) and formed reaction products (hydroquinone (HQ), benzoquinone (BQ), 1,2-dihydroxibenzene (1, 2 DHBz)), and CO₂; ^b—Phenol conversion after 6 h of reaction time (reaction conditions: 110 mL of 50 mg·L⁻¹ phenol aqueous solution, 0.05 g photocatalyst, T = 18 °C, light source AM 1.5).

The carbon balance $((C(\text{outlet})/C(\text{inlet})) \times 100)$ in our experiments was better than 92%. The Ph conversion ranged between 8.7% (for bare TiO₂) and 15.8% (for Pt/TiO₂). From the Ph conversion point of view, metal deposition enhances the activity of TiO₂ (Pt/TiO₂ > Ag/TiO₂ > Au/TiO₂ > TiO₂). The formation of Ph mild oxidation products at end of reaction time, hydroquinone (HQ), benzoquinone (BQ) and 1,2-dihydroxibenzene (1,2 DHBz), could be observed only on metal-loaded TiO₂ (Me = Ag, Au, Pt). In contrast, over bare TiO₂, Ph was mineralized directly to CO₂. The brief analysis of our results suggests that metal deposition on TiO₂ favor the formation of oxygenated products, whereas over pristine TiO₂, Ph is mineralized directly to CO₂, without intermediate formation. As we shall show in this article, the choice of metal is crucial in controlling the selectivity of oxidation reaction.

The time course of products formation during photocatalytic oxidative degradation of phenol over bare and metal-modified TiO₂ exposed to simulated solar light is presented in Figure 3. It can be observed that the formation of oxygenated products takes place

only on metal-loaded TiO_2 . The amount of HQ increases rapidly in the first hour of the reaction, then the formation rate is stabilized at $\approx 0.1 \mu\text{moles h}^{-1}$. The activity order for HQ formation over metal-loaded TiO_2 is $\text{Ag}/\text{TiO}_2 < \text{Au}/\text{TiO}_2 < \text{Pt}/\text{TiO}_2$. Transient formation of BQ was observed only over Pt/TiO_2 and Au/TiO_2 . The amount of BQ peaked at ≈ 2.3 and $0.4 \mu\text{moles}$ for the former and second photocatalysts, respectively, after 2 h of reaction. For a longer reaction time, the amount of BQ decreases progressively, vanishing completely for Au/TiO_2 and remaining at low concentration ($\approx 0.5 \mu\text{moles}$) in the case of Pt/TiO_2 .

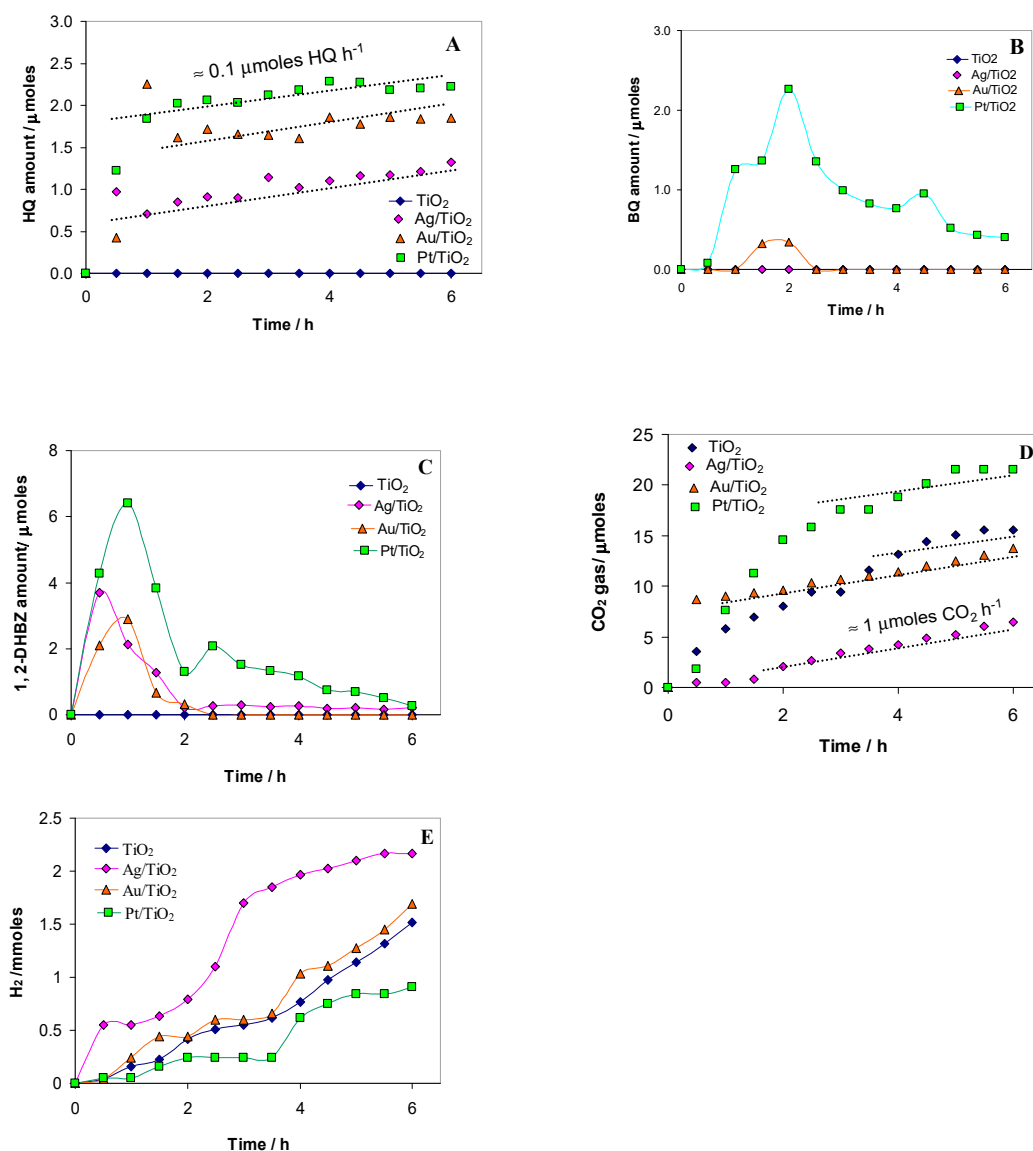


Figure 3. Solar light-driven phenol oxidative conversion to oxygenated compounds (HQ (A), BQ (B), and 1,2 DHBz (C)), CO_2 (D) and to H_2 (E) over bare and metal modified TiO_2 synthesized by laser pyrolysis. Experimental conditions: 0.05 g suspended in 110 mL of $50 \text{ mg}\cdot\text{L}^{-1}$ phenol aqueous solution, reaction temperature 18°C , simulated solar light AM 1.5.

The evolution of reaction selectivity to oxygenated compounds and CO_2 is presented in Figure 4A–E. Selectivity to 1,2 DHBz reaches a maximum at 30 min for all metal-loaded catalysts (78% for Ag/TiO_2 , 73% for Pt/TiO_2 , 53% for Au/TiO_2) (Figure 4C). Highest selectivity to oxygenated products (1,2 DHBz + HQ + BQ) of $\approx 95\%$ was measured for Pt/TiO_2 after 0.5 h of reaction time, followed by Au/TiO_2 (77% at 1 h), Ag/TiO_2 (61% at 2 h), and TiO_2 (0%) (see Figure 4E).

2.3. Noble Metals Role in Charge Separation and ROS Generation

The next step of our investigation was to elucidate in more details the role played by metals in photocatalytic oxidation processes, specifically in (i) charge separation and in (ii) ROS generation.

Electron-hole recombination is one of the main energy loss routes through radiative and nonradiative processes [19]. Photoluminescence (PL) experiments were designed to observe whether, in our case, metal deposition is effective to decrease charge recombination by PL emission.

It is documented that, PL emission intensity depends on photogenerated charge concentration [20]. The PL spectra in Figure 5 show that the energy loss by radiative recombination decreases because of metal deposition on TiO_2 , due to a better separation of photocharges at the metal–oxide interfaces [14,15]. In light of experimental results, the most efficient charge separation takes place on Au/TiO_2 , followed, in order, by Ag/TiO_2 and Pt/TiO_2 . Improvement in charge separation is expected to enhance photocatalytic activity because a greater number of electrons and holes become available for redox processes associated with photocatalytic reactions. Our results confirm that a higher conversion of Ph is observed over metal-loaded TiO_2 compared to bare TiO_2 (see Table 2). However, based only on PL emission intensity results, it is difficult to predict the precise order of activity because, beside the important role played by metals in charge separation, metals work as co-catalysts, mediating charge transfer to reacting substrates.

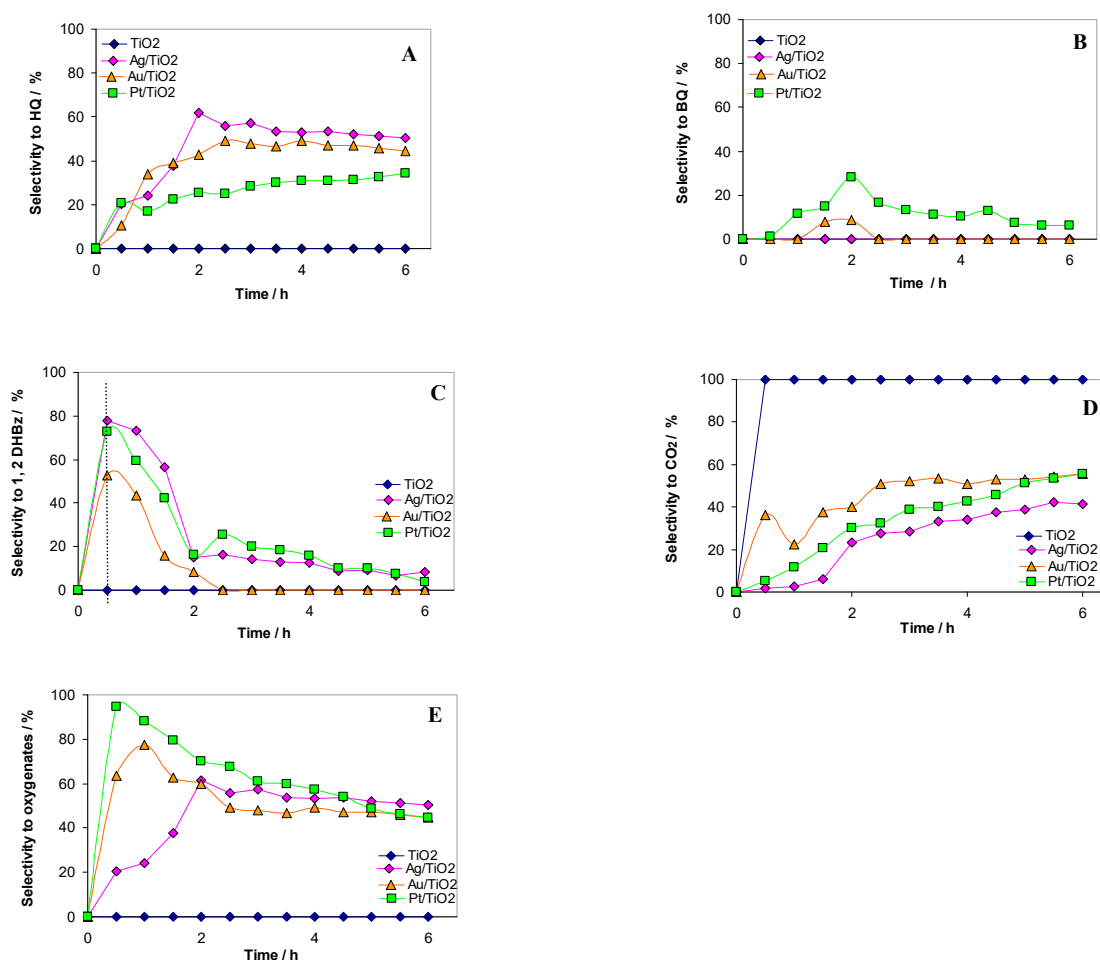


Figure 4. Time course of selectivity for phenol photocatalytic oxidative conversion to HQ (A), BQ (B), 1,2 DHBz (C), CO_2 (D) as well as overall selectivity to oxygenates (E) over bare and metal-modified TiO_2 exposed to simulated solar light.

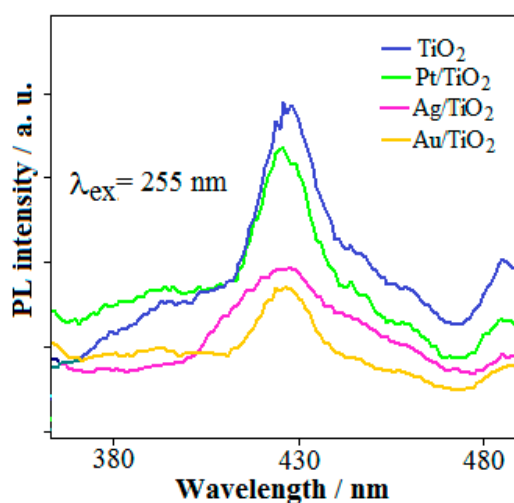


Figure 5. Comparative PL emission spectra of bare and metal-loaded TiO₂. Experimental conditions: 0.5 mg catalysts suspended by ultrasonication in 3 mL of water.

2.4. ROS Formation on Bare and Metal-Loaded TiO₂

We have considered three main reaction pathways for the oxidative conversion of Ph: (i) straight charge injection to adsorbed organic substrate on catalyst surface, (ii) reaction of organic substrate with $\cdot\text{OH}$ or with O_2^- . In case of oxidative degradation reaction mechanism, the photogenerated charges are shuttled to Ph by intermediation of ROS ($\cdot\text{OH}$ and O_2^-). It is well documented that $\cdot\text{OH}$ is a powerful, non-selective, oxidant, whereas O_2^- is a weak oxidant [21].

To get further information on the relationship between ROS formation and the photocatalytic behavior of our materials, we have assessed the formation of $\cdot\text{OH}$ and O_2^- under light irradiation by using selective radical quenchers.

The formation of free $\cdot\text{OH}$ radicals was probed by monitoring the development of fluorescent umbelliferone resulted in the reaction between non-fluorescent coumarin and $\cdot\text{OH}$ radicals. The amount of $\cdot\text{OH}$ raises gradually in time, for all photocatalyst exposed to solar light (see Figure 6A,B). From data presented in Figure 6B, the estimated amounts of $\cdot\text{OH}$ formed in 6 h of irradiation time in 110 mL of solution of reactor are: Pt

TiO_2 (168 $\mu\text{moles g}^{-1}_{\text{cat}}$) > TiO_2 (156 $\mu\text{moles g}^{-1}_{\text{cat}}$) \approx Au/TiO_2 (155 $\mu\text{moles g}^{-1}_{\text{cat}}$) > Ag/TiO_2 (131 $\mu\text{moles g}^{-1}_{\text{cat}}$). From comparison with photocatalytic data, it comes out that the $\cdot\text{OH}$ quantity is proportional with that of CO_2 . The experimentally measured CO_2 , after of 6 h of reaction time, over 0.05 g of photocatalysts, was: Pt/TiO_2 (430 $\mu\text{moles g}^{-1}_{\text{cat}}$) > TiO_2 (310 $\mu\text{moles g}^{-1}_{\text{cat}}$) \approx Au/TiO_2 (276 $\mu\text{moles g}^{-1}_{\text{cat}}$) > Ag/TiO_2 (128 $\mu\text{moles g}^{-1}_{\text{cat}}$) (see comparatively Figures 6B and 4D). Taking into account that the probability of $\cdot\text{OH}$ trapping by coumarin or by Ph vary as a function of experimental conditions [22], it can be observed, based on the good matching between radical quenching and photocatalytic results, that CO_2 formation relates to $\cdot\text{OH}$ production. The plots in Figure 6C show a clear correlation between relative amounts of $\cdot\text{OH}$ and CO_2 formed over the investigated materials. Therefore, we assume that $\cdot\text{OH}$ radicals are responsible for the mineralization of Ph to CO_2 (non-selective oxidation route). The formation of CO_2 cannot be prevented over TiO_2 -based materials dispersed in aqueous media because the formation of $\cdot\text{OH}$ radicals is unavoidable.

The formation of O_2^- over metal loaded TiO_2 was evidenced indirectly by detection of formazan, which is the product of reaction between XTT and O_2^- . The specific absorbance peak of formazan is at 485 nm (Figure 7A). The reduction efficiency of O_2 to O_2^- , estimated from the amount of formazan, decreases in the order Pt/TiO_2 > Au/TiO_2 > Ag/TiO_2 (Figure 7B). The formation of O_2^- could not be evidenced via formation of formazan on the bare TiO_2 sample, prepared by laser pyrolysis. There are, however, reports claiming that O_2^- is formed on TiO_2 . For example, Goto et al. [23] detected the formation of O_2^-

on rutile particles, suggesting that electron transfer takes place from an organic moiety (2-propanol) to O_2 .

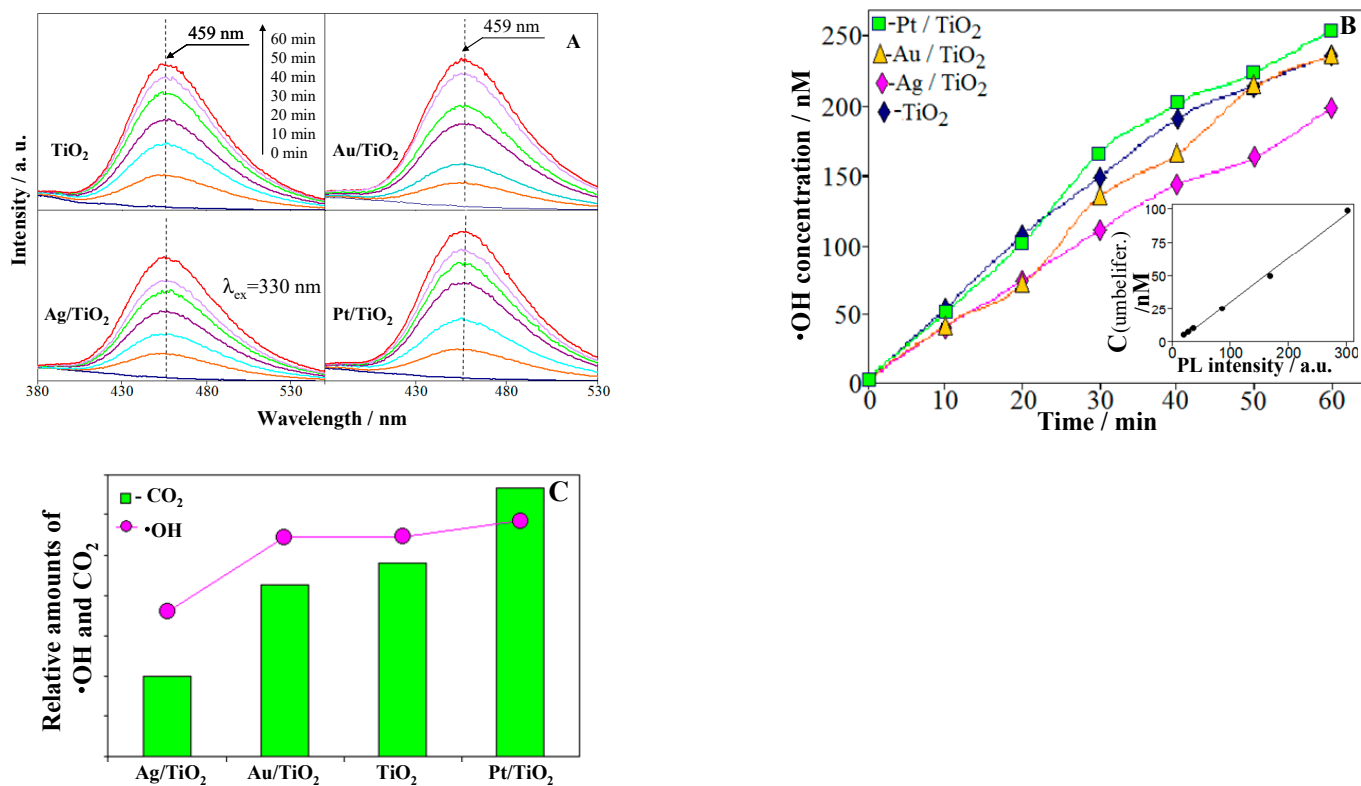


Figure 6. Time course of umbelliferone PL (A) and evolution in time of $\cdot OH$ concentration (B) over the investigated photocatalysts exposed to solar light, as well as the relative amounts of CO_2 and $\cdot OH$ formed over the photocatalysts exposed to simulated solar light for 6 h (C). The formation of $\cdot OH$ radical was evidenced by observing PL peak of umbelliferone at ≈ 450 nm for $\lambda_{exc} = 330$ nm (coumarin traps selectively $\cdot OH$ to form umbelliferone). Inset of figure B represents the calibration curve obtained by plotting the PL response against umbelliferone concentration. Experimental conditions: 1 mg catalyst was dispersed by ultrasonication in 40 mL of 11 mM coumarin solution and then exposed to simulated solar light AM 1.5.

The quantity of oxygenated products resulted by photocatalytic oxidation of Ph scale with the relative amounts of O_2^- (see Figure 7C). From here, it comes that, O_2^- is the ROS responsible for Ph mild oxidation. The main outcomes from O_2^- quenching experiments are: (i) supported metals catalyze O_2^- formation and (ii) O_2^- is the main player in Ph mild oxidative route. The eventual role played by O_2^- for degradation of oxygenated compounds to CO_2 should not be completely disregarded, although O_2^- is a significantly weaker oxidant compared to $\cdot OH$. The BQ is indicated as an effective O_2^- quencher [1]. We have observed indeed the rapid degradation of BQ, formed only over Pt/TiO₂ and Au/TiO₂ (see Figure 3B).

The formation of ROS was checked also in visible light domain ($\lambda > 420$ nm).

The results of Figure 8 show that, the formation of $\cdot OH$ radical does not proceed under visible light for any of the investigated materials (Figure 8), which is in line with the absence of CO_2 formation during photocatalytic tests conducted in visible light. Our selective radical quenching results demonstrate that CO_2 formation is due to $\cdot OH$ appearance.

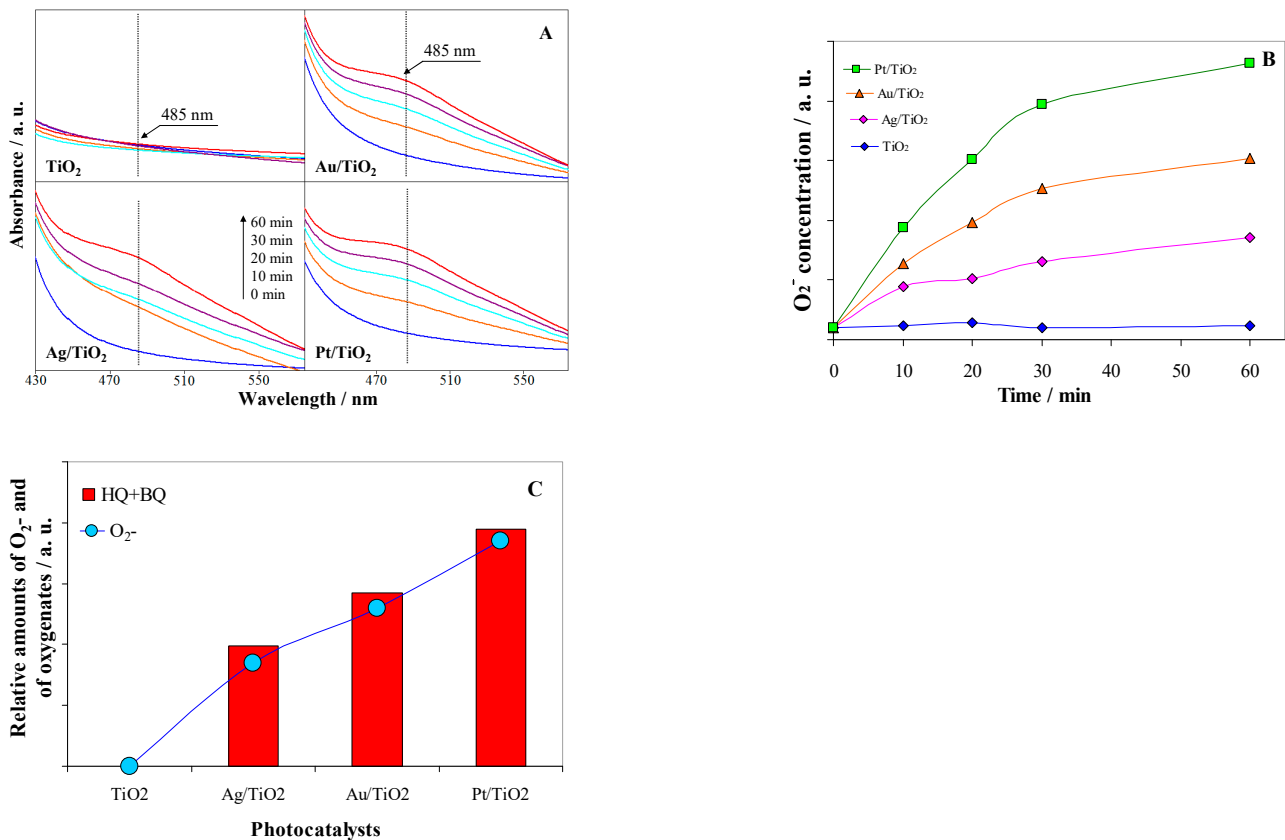


Figure 7. Time course of formazan absorbance (A), formed in the reaction between O₂⁻ and XTT probe molecule, and evolution of O₂⁻ relative concentration over the catalysts exposed to solar light (B). Relative amounts of oxygenates (HQ + BQ) measured at end of reaction in comparison with that of O₂⁻ (C). Experimental conditions: 4 mg of catalysts, dispersed into 3 mL of XTT sodium salt solution, were exposed to simulated solar light to induce the formation formazan, which was put in evidence by the UV-VIS absorption peak at ≈ 470 nm.

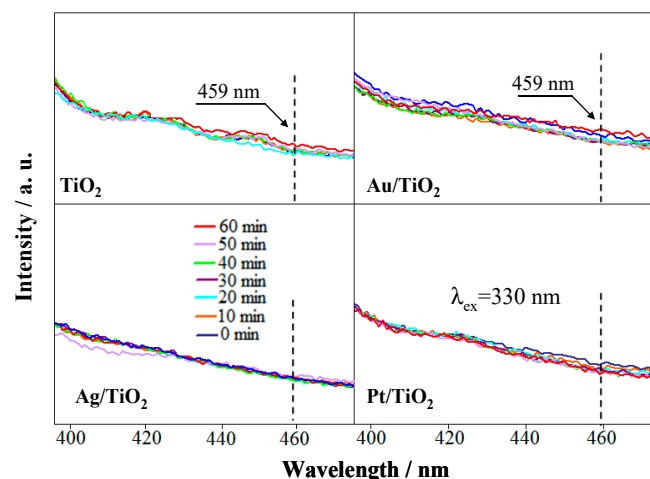


Figure 8. Coumarin formation survey, indicative of ·OH radical formation, upon exposure to visible light ($\lambda > 420$ nm) of catalysts dispersed in aqueous media.

The survey conducted in visible light ($\lambda > 420$ nm) reveal that O₂⁻ formation does not take place over the scrutinized materials with exception of Au/TiO₂ (Figure 9). The formation of O₂⁻ takes place by reaction between hot electrons of Au plasmon and adsorbed O₂ in vicinity of Au nanoparticles [14]. Participation of TiO₂ in O₂⁻ formation, via Au plasmon electron injection in TiO₂ conduction followed by O₂ reduction on TiO₂, was

also suggested [24]. However, the very short lifetime of plasmons of 2–10 fs associated with the low energy of electrons [25,26] decrease the probability of O_2^- reduction. We have observed experimentally only tiny amounts of O_2^- formed under visible light exposure of Au/TiO₂, which are not enough to react with Ph at rates high enough to make possible the identification of mild oxidation reaction products by HPLC. The catalytic test results, carried out over all photocatalysts at $\lambda > 420$ nm, evidenced the formation of small amounts of H₂ only over Au/TiO₂ (≈ 2.5 μ moles in 5 h of reaction). The experiments performed in visible light show that ROS are not produced, because visible light ($\lambda > 400$) nm is not absorbed by TiO₂.

In the UV region, both $\cdot OH$ radicals and O_2^- are produced, the former on TiO₂ and the second on metals. The $\cdot OH$ oxidizes non-selectively the organic substrate(s) to CO₂ and H₂O. The reactions implying $\cdot OH$ participation are important for environmental applications, where the scope is to mineralize rapidly the organic pollutant to non-harmful CO₂. In our case, the mild oxidant O_2^- , is produced only on supported noble metal particles, only under exposure to UV light. In addition to radical trapping experiments, the results of our photocatalytic tests evidence that, CO₂ is the only reaction product of phenol oxidation over bare TiO₂. The metals mediate the transfer of the photogenerated electrons from TiO₂ to adsorbed O₂. The activity order for O_2^- formation is Pt/TiO₂ > Au/TiO₂ > Ag/TiO₂ (TiO₂ shows no activity). The interplay between material activity for $\cdot OH$ and O_2^- production determines the catalyst selectivity to oxygenated products and CO₂. Pt/TiO₂ is the most active to produce both $\cdot OH$ and O_2^- , thus it will give finally the best phenol conversion. This result proves that Pt/TiO₂ generates the highest amount of photogenerated charges ready to participate in redox processes. The Ag/TiO₂ is the less active generator of $\cdot OH$ and O_2^- and consequently shows the smallest phenol conversion among metal-loaded photocatalysts. The supported metals have certain influence on activity of TiO₂ support to produce $\cdot OH$: Pt/TiO₂ > TiO₂ \approx Au/TiO₂ > Ag/TiO₂. Pt on TiO₂ enhances the formation rate of $\cdot OH$ compared to bare TiO₂, whereas Ag depresses it. Supported Au seems to have no influence on activity of TiO₂ for $\cdot OH$ formation.

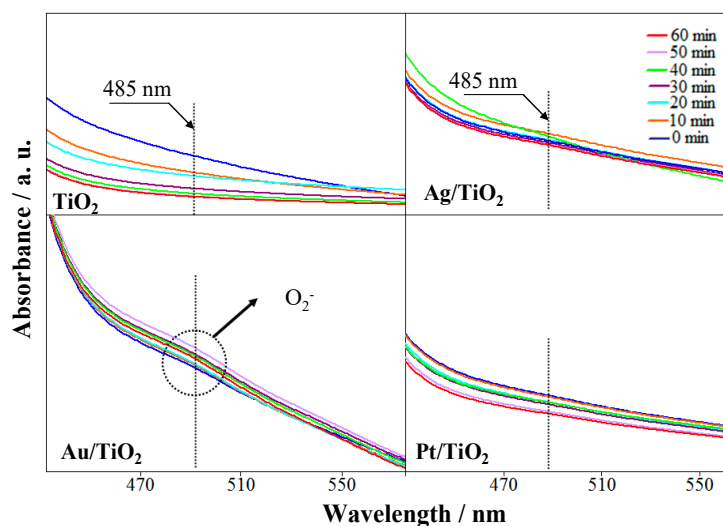


Figure 9. Survey of O_2^- production, by monitoring formazan specific absorbance, over the catalysts exposed to visible light ($\lambda > 420$ nm).

In visible region ($\lambda > 420$ nm), both catalyst types (bare and metal-loaded TiO₂) show negligible photocatalytic activity because neither $\cdot OH$ nor O_2^- are produced. The tiny amounts of O_2^- generated on Au/TiO₂ are originate from Surface Plasmon Resonance (SPR) shown by Au nanoparticles. Hot electrons on surface of Au particles reduce small amount of O₂. The absence of ROS production in visible light is most likely due to the fact that the light absorption edge is at 400 nm (see the UV-VIS spectra in Figure 2), consistent

with a band gap of ≈ 3.1 eV. The visible light absorbed by Ag/TiO₂ and Au/TiO₂ is capable of triggering the formation of tiny amounts of O₂^{•−} by electron donation to adsorbed O₂, only in case of Au/TiO₂ (see Figure 9).

To get additional experimental evidence on the nonselective Ph degradation route by •OH radicals, we have designed a new series of experiments, aiming to hinder the formation of umbelliferone from coumarin. The concentration of Ph was chosen to be high enough (2 mM) to consume the majority of •OH radicals formed in 30 min of exposure to light, thus lowering the probability of coumarin to quench •OH radicals. In this way, the photoluminescence of umbelliferone was expected to diminish in presence of Ph.

The results of Figure 10 confirm that the •OH radicals produced by TiO₂ are able to react with Ph. When the concentration of Ph is small (0.2 mM), the •OH radicals react preferentially with coumarin, yielding the photoluminescent umbelliferone. When Ph concentration is raised to 2 mM, the formation of umbelliferone is depressed by the competing reaction between •OH and Ph (see orange trace in Figure 10). In case of Au/TiO₂ and Ag/TiO₂ catalysts, the small residual PL maxima indicate that tinny amount of •OH radicals are still able to react with coumarin even in presence of Ph in high concentration. Other studies [27] reported that the addition of alcohols have only a limited influence on umelliferone formation because the alcohols are preferentially adsorbed and oxidized by holes on the surface of the photocatalyst, without significant interference of •OH radicals.

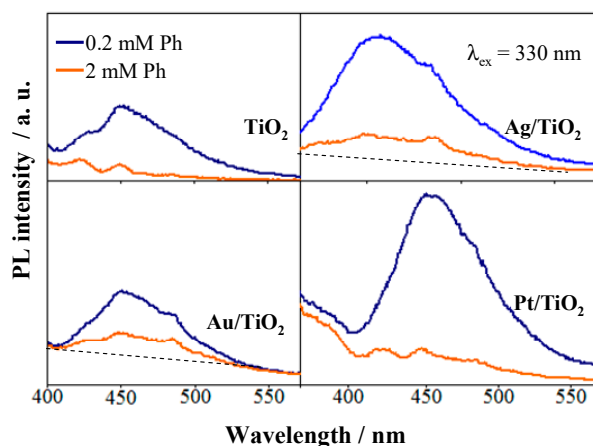


Figure 10. The survey of •OH formation in low (trace 0.2 mM Ph) and high Ph concentration (trace 2 mM Ph) over photocatalyst exposed to simulated solar light for 30 min. Experimental conditions: 0.6 mg photocatalyst was dispersed by ultrasonication in 40 mL solution of coumarin (11 mM)-Ph (0.2 mM) (blue trace 0.2 mM). In second case, the concentration of Ph in 11 mM coumarin solution was increased to 2 mM (orange trace 2 mM).

2.5. Photoelectric Properties of Bare and Metal-Modified TiO₂

It is documented that the energies of valence and conduction bands of metal-modified semiconductors are shifted upward with a value depending on the height of the Schottky barrier, forcing the electrons and holes to move in different directions [14,28]. The quick charge carrier recombination, the time scale varying from μ s to ns [29], is hindered, allowing the time for a charge transfer to occur at the interface. The space separation of photogenerated charge carriers inherently leads to the appearance of a certain surface photovoltage (SPV), the measurement of which can provide valuable information concerning the transfer dynamic of such carriers [30–32]. Thus, it was previously demonstrated that, for an n-type semiconductor, photoinduced electrons migrate towards the illuminated side of the material, giving rise to a negative SPV signal. Conversely, a positive SPV signal corresponds to a p-type semiconductor, in which case holes are directed from the surface to the bulk [33,34]. However, in both cases the surface photovoltage is wavelength dependent, being affected by the particular features of the semiconducting material, in terms of light absorption and transport of excess carriers [35,36].

The surface photovoltage was measured for each sample at several wavelengths and, as expected, SPV spectra (Figure 11) revealed in all the cases an n-type semiconducting character. Obviously, SPV signals measured under the actual experimental conditions correspond, in fact, to the potential difference between the Fermi level of ITO (indium tin oxide, +0.35 V vs. NHE [34]) and that of the irradiated sample. Since the conduction band of non-stoichiometric TiO_2 is located above its Fermi level with an average value of ca. 0.5 V [37], and by taking into account a value of around -0.33 V for the O_2/O_2^- level [1], it appears that the formation of O_2^- species at the surface of the irradiated samples requires an SPV value higher than ca. -0.18 V. As the results from Figure 11 indicate, this condition is not fulfilled in the case of pristine TiO_2 , whereas at noble metal-modified samples O_2^- formation is possible, at least in principle, for irradiation wavelengths lower than 380 nm. Nevertheless, the probability for this process increases with SPV signal, in the order $\text{Pt}/\text{TiO}_2 > \text{Au}/\text{TiO}_2 > \text{Ag}/\text{TiO}_2$, as schematically illustrated in the inset in Figure 11. These findings are in excellent agreement with the activity for O_2^- formation deduced from radical quenching experiments (see Figure 7).

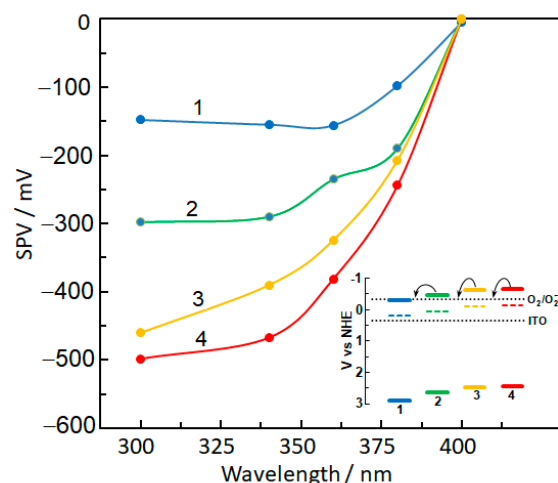


Figure 11. Surface photovoltage (SPV) spectra of pristine TiO_2 (1), Ag/TiO_2 (2), Au/TiO_2 (3), and Pt/TiO_2 (4). Inset: corresponding energy diagram at 300 nm; the dashed lines indicating the Fermi levels of samples.

To emphasize the effect of noble metal modification of the titanium oxide on the O_2^- generation process, chronoamperometric experiments were performed in dark, at an applied voltage of -1 V. Figure 12 shows the time-variation of the oxygen reduction current, estimated as the difference between the current recorded in O_2 atmosphere and that observed under Ar conditions. For easier comparison, the currents were expressed in terms of mass activity (oxygen reduction current normalized to the amount of the investigated powder sample). Pristine TiO_2 exhibited negligible response (see curve 1 from Figure 12), which clearly demonstrates that the presence of noble metal particles is a prerequisite for O_2 reduction. It was interesting to observe that, up to ca. 50 s, the current recorded at Au/TiO_2 is higher than that at Pt/TiO_2 , although during further polarization the decrease in the current tends to become much slower for the latter (compare curves 3 and 4 from Figure 12). To better put into perspective the role of the noble metal nature, inset (a) in Figure 12 illustrates the decay of the oxygen reduction current on a log–log scale. Linear dependences were found in all cases, which could indicate a Langmuir adsorption kinetic control of O_2 on the overall reduction process [38]. However, Pt/TiO_2 exhibited the slowest current decrease, whereas for Au/TiO_2 a change in slope was observed, the decline of the current becoming much steeper after only ca. 10 s, probably as result of a more sluggish adsorption of oxygen reactant species. Consequently, after about 200 s of continuous polarization, oxygen reduction current at Pt/TiO_2 is more than twice as high as that observed with Au/TiO_2 . These results are important because they can provide

an explanation for the fact that, compared to the case of Au/TiO₂, the total amount of O₂[−] produced at Pt/TiO₂ is much higher (see inset in Figure 12) than would have been expected for rather small difference in terms of SPV signals between the two materials. Integration of the current responses from Figure 13 over the entire polarization time, yielded oxygen reduction charges of ca. 0.78, ca. 1.10, and ca. 1.46 mC g^{−1} for Ag/TiO₂, Au/TiO₂, and Pt/TiO₂, respectively. As illustrated by the inset (b) in Figure 12, based upon these values, corresponding amounts of O₂[−] species of 7.8, 11.4, and 15.2 nmol g^{−1} were estimated as being formed at the investigated active samples. The maximum amount of oxygenated compounds (HQ + BQ + 1,2 DHBz) formed over Ag/TiO₂ (4.7 μmoles), Au/TiO₂ (5.1 μmoles), and Pt/TiO₂ (9.5 μmoles) after 1 h of reaction time (0.5 h in case of Ag/TiO₂), follows closely the tendency observed in polarization measurements of O₂ reduction (Figure 12). The precise correlation between quantitative polarization and photocatalytic data concerning oxygenated compounds is difficult because the formation and depletion of O₂[−] by reaction with organic substrate(s) is a dynamic process compared to O₂ adsorption on polarized surface. To build up a reliable kinetic, it is necessary to find out the rate of O₂[−] formation in reaction conditions. However, a close relationship between formation of O₂[−] species and mild oxidation of Ph is demonstrated by two independent experimental techniques (selective radical trapping and chronoamperometric experiments).

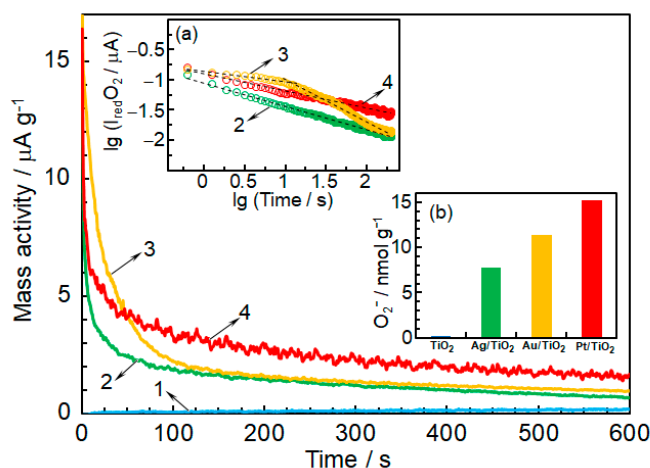


Figure 12. Time-variation of the mass activity for oxygen reduction at pristine TiO₂ (1), Ag/TiO₂ (2), Au/TiO₂ (3), and Pt/TiO₂ (4), at an applied voltage of -1 V. Insets: (a), log–log plots for the oxygen reduction current decay at noble metal-modified TiO₂; (b), estimated O₂[−] amounts formed during 10 min of continuous polarization.

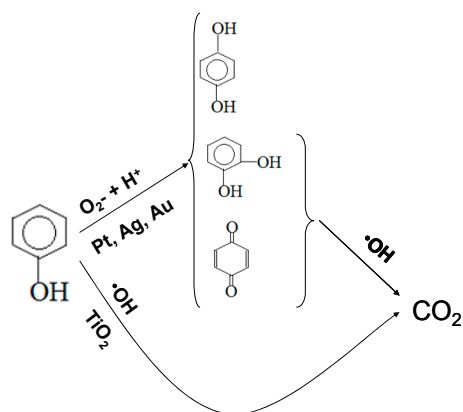


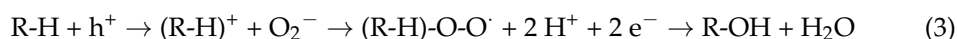
Figure 13. Distinct mechanisms of Phenol (Ph) photocatalytic oxidative conversion over bare and noble metal-modified TiO₂.

The corroboration of entire experimental evidences collected in this research lead to the reaction scheme presented below.

We assumed, based on experimental facts, that Ph is oxidized non-selectively by $\cdot\text{OH}$ radicals directly to CO_2 , apparently without producing in our experimental conditions detectable long-lived intermediates. Supported noble metals are responsible for O_2 reduction to O_2^- , by mediating the transfer of photoelectron from TiO_2 to adsorbed O_2 . The subsequent O_2^- reaction with Ph leads to formation of oxygenated products (HQ, BQ, 1,2 DHBz). The literature focuses mostly on reactivity O_2^- in organic protic and aprotic solvents and less on the reactivity in aqueous solutions [21]. However, it is recognized that, O_2^- disproportionates spontaneously in water, forming O_2 and hydroperoxide anion (HO_2^-). One possibility is that the reaction follows the superoxide dismutase (SOD) pathway (Equation (1)), proposed to explain the biological function of superoxide ion [39]:



Equation (2) suggests that the insertion of oxygen in ortho and para position takes place by the reaction of organic substrate with H_2O_2 in vicinity or on supported noble metal(s). Alternatively, the oxidation mechanism may occur through activation of Ph by transfer of photogenerated hole followed by nucleophil attack of O_2^- to generate organic peroxy radicals which react further with H^+ and e^- to form finally the hydroxylated organic compound (see Equation (3)) [40].



Actually, there is a limited knowledge on the reaction mechanism concerning the interaction in aqueous media between the adsorbed O_2^- and organic substrate in the presence of a catalytic metal. The published literature gives no information on the eventual role played an active metal in the above proposed reaction mechanisms.

3. Experimental

3.1. Preparation of Catalytic Materials

The photocatalysts employed in this study are TiO_2 , Pt/TiO_2 , Ag/TiO_2 , and Au/TiO_2 . High surface area TiO_2 , formed of nanometric sized particles, were prepared by laser pyrolysis using TiCl_4 as precursor material. The detailed experiential setup and procedures are described elsewhere [41]. Metal deposition was performed by impregnating TiO_2 with H_2PtCl_6 , AgNO_3 , and HAuCl_4 precursors followed by reduction with NaBH_4 [42]. For additional information on preparation of photocatalytic materials, see the Supplementary Information. Finally, the catalysts were dried and calcined 100 and 300 °C, respectively. The elemental composition, identification of crystalline phases and measurements of average crystallite size of photocatalytic materials was made by Energy Dispersive X-ray analysis (EDAX) and XRD, respectively. In the case of Pt/TiO_2 , the dispersion and average Pt particle size was estimated by CO chemisorption measurements, carried out with a ChemBet–3000 Quantachrome Instrument (Odelzhausen, Germany) equipped with a thermal conductivity detector (TCD) apparatus [43].

The values of optical band gap are estimated from the Tauc plots of diffuse reflectance UV-VIS data converted into absorbance by Kubelka–Munk function [44].

The X-ray Photoelectron Spectroscopy (XPS) measurements were performed in an ESCALAB Xi+ (Thermo SCIENTIFIC Surface Analysis, Baltimore, MD, USA) setup equipped with a multichannel hemispherical electron Analyzer (dual X-ray source) working with Al $\text{K}\alpha$ radiation ($h\nu = 1486.2 \text{ eV}$), using C 1s (284.8 eV) as the energy reference. The chemical compositions of surface and oxidation states were estimated from the XPS spectra by calculating the integral of each peak after subtraction of the “S-shaped” Shirley-type background using the appropriate experimental sensitivity factors.

The Photoluminescence (PL) emission spectra were recorded with Cary Eclipse Fluorescence Spectrophotometer (Agilent Technologies, Santa Clara, CA, USA) apparatus [45].

Experimental setup for photocatalytic tests. Photocatalytic experiments were conducted in a batch-type photo reactor depicted in Figure 14. The AM 1.5 (1000 W m^{-2}) light beam of $4.5 \times 4.5 \text{ cm}^2$ was provided by a solar light simulator (Pecell-L01, Yokohama, Japan) equipped with a 150 W xenon short-arc lamp. The double-walled photoreactor was provided with optical degree quartz window. For each test, 110 mL of $50 \text{ mg}\cdot\text{L}^{-1}$ phenol aqueous solution containing the suspended catalyst powder (0.05 g) were placed into the photoreactor, thermostated at $18 \text{ }^\circ\text{C}$ with a chiller. Prior tests, the suspension was kept in dark for 30 min, under stirring, to attain equilibration of experimental system. Typically, one experiment consisted of light irradiation of liquid-suspended photocatalysts for 360 min.

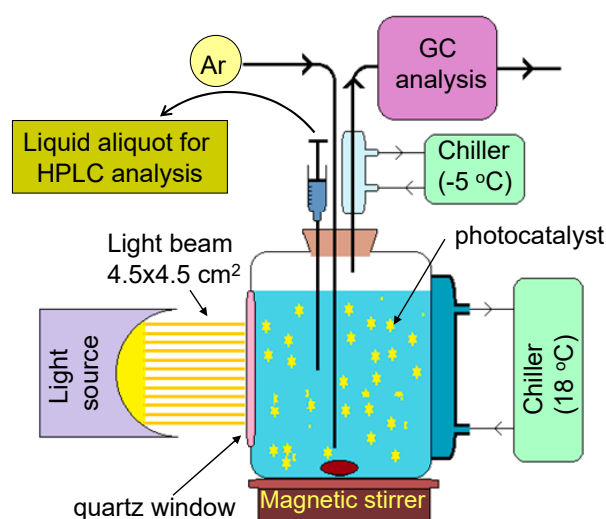


Figure 14. Experimental setup used for photocatalytic tests composed of quartz reactor provided with quartz window, AM 1.5 light source, liquid and gas sampling systems, gas and liquid chromatographs, and chillers to control the temperatures of glass condenser ($-5 \text{ }^\circ\text{C}$) and of reactor ($18 \text{ }^\circ\text{C}$).

During tests, the Ar carrier gas was purged continuously into the phenol aqueous solution at a flow rate of $10 \text{ mL}\cdot\text{min}^{-1}$, passed through a refrigerant cooled to $-5 \text{ }^\circ\text{C}$ with a chiller to remove liquid vapors, and then sent to GC for on-line composition analysis at 30 min time interval with a gas chromatograph (Buck Scientific, Norwalk, CT, USA) equipped with TCD detectors. The H_2 and O_2 were separated and quantified on Molecular Sieve 5 \AA , whereas CO_2 and the eventually formed C_2H_6 and C_2H_4 on the Hayesep column. Meanwhile, aliquots of 2 mL were extracted every 30 min from the liquid phase, filtered through $0.22 \text{ }\mu\text{m}$ Q-Max membrane filter, and then injected for analysis into a liquid chromatograph (Alliance e2659, Waters, Milford, MA, USA). The organic components of liquid phase (phenol (Ph), hydroquinone (HQ), benzoquinone (BQ), and 1,2-dihydroxibenzene (1,2 DHBz)) were separated on HPLC column (C18- $3.5 \text{ }\mu\text{m}$ Symmetry, Waters), identified, and then quantified using the UV-VIS detector set at 273 nm. The mobile phase of HPLC (isocratic elution program) was a mixture of Milli-Q ultrapure water ($18 \text{ M}\Omega$) and methanol ($80/20 \text{ v/v}$). The flow rate of the mobile phase was $1 \text{ mL}\cdot\text{min}^{-1}$ and the sample injection volume was $2 \text{ }\mu\text{L}$.

3.2. Detection of $\cdot\text{OH}$ Radicals

Coumarin was used as selective trap for the $\cdot\text{OH}$ radicals formed under photocatalysts exposure to light [12,27]. The 0.001 g of powder catalysts were first suspended in 40 mL of 11 mM coumarin (Merck) aqueous solution and then exposed either to simulated solar light AM 1.5 or to visible light. A cut off filter (L42, Asahi Spectra, California, USA) was in the

case of visible light ($\lambda > 420$ nm). Aliquots of 1.5 mL solution were sampled at 10 min time interval for fluorescence measurements (Cary Eclipse Fluorescence Spectrophotometer, Agilent Technologies, Santa Clara, CA, USA) to monitor umbelliferone, formed by reaction between coumarin and $\cdot\text{OH}$ radicals. Umbelliferone gives a specific fluorescence peak at ≈ 450 nm for $\lambda_{\text{exc}} = 330$ nm.

3.3. Detection of O_2^-

In a typical experiment, 0.004g of catalyst was suspended into 4 mL of 3 mM solution of XTT sodium salt (2, 3-bis(2-methoxy-4-nitro-5-sulfophenyl)-2H-tetrazolium-5-carboxanilide) (Alfa Aesar). Then, the samples were exposed to simulated solar or visible light for 10, 20, and 30 min to induce the formation of O_2^- . XTT reduction by O_2^- produces XTT-formazan, which can be evidenced by a broad absorption peak at ≈ 470 nm [12,44]. The measurements were carried out with UV-VIS spectrophotometer (Analytik Jena Specord, 200 Plus, Jena, Germany).

For the surface photovoltage (SPV) measurements, a sandwich-like photovoltaic cell was built, according to a method previously described in the literature [30]. Briefly, a small amount (ca. 12 mg) of pristine or metal-modified titanium oxide was firmly pressed in between two ITO electrodes, to obtain a confined film composed of the investigated powder sample. The upper face of the cell was irradiated (under chopped conditions) with a monochromatic light (the light beam of 300 W Xe lamp of Asahi Spectra MAX-350 (Tokyo, Japan) light source was passed through high transmission bandpass filters with FWHM = 11 nm) and the SPV signal was measured by means of a computer-driven Keithley 2425 source-meter (Cleveland, Ohio, USA). The energy of the monochromated light beam was measured with Newport optical power meter (Model 1830-R, Irvine, CA, USA) equipped a calibrated photodiode detector (Newport, 918D series). For the chronoamperometric experiments, the same cell was used and the measurements were carried out in an air-tight reactor by means of a PAR 273A (Princeton Applied Research Walpole, MA, USA) potentiostat, both under pure O_2 and Ar atmospheres.

4. Conclusions

This study gives a comprehensive view on the light-initiated photocatalytic oxidation pathways of a model organic substrate with an aromatic ring (Ph) over bare and noble metal-loaded TiO_2 . The analysis of complex phenomena associated with photocatalytic reaction focuses on particular roles played by oxide support and by noble metals on light absorption, charge separation, formation of ROS ($\cdot\text{OH}$ and O_2^-), as well as on reaction mechanism of oxidative conversion of Ph.

We have found out that TiO_2 support generates only $\cdot\text{OH}$ as ROS when it is exposed to light with $\lambda < 400$ nm. These radicals are responsible for deep oxidation of Ph directly to CO_2 , apparently without the formation of detectable long-lived intermediates. The formation of $\cdot\text{OH}$, and consequently the photocatalyst activity, cease in visible light domain.

Deposited noble metals (Ag, Au, Pt) (i) adsorb the visible light (SPR phenomenon), (ii) assist effectively the charge separation, and the (iii) O_2 reduction to O_2^- . The deposited metal raises the Fermi level of TiO_2 allowing the reduction of adsorbed O_2 to O_2^- . The O_2^- produced on metals oxidizes mildly Ph to oxygenated products (HQ, BQ, 1,2 DHBz). In a parallel process, $\cdot\text{OH}$ radicals produced by TiO_2 support mineralize Ph directly to CO_2 by fast reaction sequences. At this stage, it is not clear the precise function of metals in the reaction between organic substrate (Ph) and O_2^- . With the exception of Au, the hot electrons produced by SPR at $\lambda > 400$ nm are not active to produce measurable amounts of O_2^- .

This study demonstrates, by two complementary experimental methods (radical quenching and photo electrochemical measurements), that production of $\cdot\text{OH}$ and O_2^- over the investigated catalysts correlates well with the activity showed for oxidative conversion of Ph. According to our data, the oxidation of Ph by photo charges is intermediated by ROS.

In light of our results, the bare TiO₂ suits the best the photocatalytic depollution purposes, where the aim is to mineralize the harmful organic substrate to CO₂. When noble metals are deposited on TiO₂, intermediate oxygenated compounds are formed by mild oxidation of organic substrate(s) by O₂[−], via photo induced electron transfer from metals to O₂. Thus, from a depollution point of view, the modification of TiO₂ with noble metals is not beneficial. In addition, the metal-modified photocatalyst in powder form dispersed in water can be harmful to the environment. Same assessment can be made for photo water splitting, where the consumption of photo-generated electron by adsorbed O₂ hinders H⁺ reduction. On the other hand, should be the practical aim of valuable oxygenated compounds synthesis by mild selective oxidation of organic compounds, the use of catalytic metals is mandatory.

Supplementary Materials: The following are available online at <https://www.mdpi.com/article/10.3390/catal11040487/s1>, Figure S1: High resolution XPS spectra of TiO₂ in O1s and Ti2p binding energy regions, Figure S2: High resolution XPS spectra of Ag/TiO₂ in O 1s, Ti 2p and Ag 3d binding energy regions, Figure S3: High resolution XPS spectra of Au/TiO₂ in O 1s, Ti 2p and Au 4f binding energy regions, Figure S4: S4 High resolution XPS spectra of Pt/TiO₂ in O 1s, Ti 2p and Pt 4f binding energy regions, Figure S5: Comparative XRD diffraction patterns of simple and metal-modified TiO₂. •-anatase, +-rutile, Table S1: Elemental composition obtained from EDAX analysis of simple and metal -modified TiO₂, Table S2: XPS survey of elemental composition of simple and noble metal-modified TiO₂, Table S3: Chemical state of titanium in the investigated materials, Table S4: Crystalline phase composition and average crystallite size of simple and metal-modified TiO₂.

Author Contributions: Conceptualization, I.B., Investigation, A.S., C.A., F.P., M.R., A.V., T.S., M.S., C.F., C.N.M., V.S.T., N.S., M.Z. and I.B., Methodology, A.S., C.A., F.P., M.R., A.V., T.S., M.S., C.F., C.N.M., V.S.T., N.S., M.Z. and I.B., Resources, A.S., C.A., F.P., M.R., A.V., T.S., M.S., C.F., C.N.M., V.S.T., N.S., M.Z. and I.B., Supervision, N.S. and I.B., Visualization, I.B., Writing—original draft, N.S. and I.B., Writing—review & editing, N.S. and I.B. All authors have read and agreed to the published version of the manuscript.

Funding: This research received no external funding.

Acknowledgments: This work was supported by Grants 46 PCCDI/2018 MALASENT.

Conflicts of Interest: The authors declare no conflict of interest.

References

1. Li, X.; Xie, J.; Jiang, C.; Yu, J.; Zhang, P. Review on design and evaluation of environmental photocatalysts. *Front. Environ. Sci. Eng.* **2018**, *12*, 14. [[CrossRef](#)]
2. Paz, Y. Application of TiO₂ photocatalysis for air treatment: Patents' overview. *Appl. Catal. B* **2010**, *99*, 448–460. [[CrossRef](#)]
3. Shaham-Waldmann, N.; Paz, Y. Away from TiO₂: A critical minireview on the developing of new photocatalysts for degradation of contaminants in water. *Mat. Sci. Semicond. Process.* **2016**, *42*, 72–80. [[CrossRef](#)]
4. Di Paola, A.; García-López, E.; Marci, G.; Palmisano, L. A survey of photocatalytic materials for environmental remediation. *J. Hazard. Mater.* **2012**, *211*, 3–29. [[CrossRef](#)]
5. Chen, L.; Tang, J.; Song, L.N.; Chen, P.; He, J.; Au, C.T.; Yin, S.F. Heterogeneous photocatalysis for selective oxidation of alcohols and hydrocarbons. *Appl. Catal. B* **2019**, *242*, 379–388. [[CrossRef](#)]
6. Meng, S.; Ye, X.; Zhang, J.; Fu, X.; Chen, S.; Chen, S. Effective use of photogenerated electrons and holes in a system: Photocatalytic selective oxidation of aromatic alcohols to aldehydes and hydrogen production. *J. Catal.* **2018**, *367*, 159–170. [[CrossRef](#)]
7. Kou, J.; Lu, C.; Wang, J.; Chen, Y.; Xu, Z.; Varma, R.S. Selectivity Enhancement in Heterogeneous Photocatalytic Transformations. *Chem. Rev.* **2017**, *117*, 1445–1514. [[CrossRef](#)] [[PubMed](#)]
8. Hou, W.; Cronin, S.B. A Review of Surface Plasmon Resonance-Enhanced Photocatalysis. *Adv. Funct. Mater.* **2013**, *23*, 1612–1619. [[CrossRef](#)]
9. Carp, O.; Huisman, C.L.; Reller, A. Photoinduced reactivity of titanium dioxide. *Progress Solid State Chem.* **2004**, *32*, 33–177. [[CrossRef](#)]
10. Fujishima, A.; Rao, T.N.; Tryk, D.A. Titanium Dioxide Photocatalysis. *J. Photochem. Photobiol. C Photochem. Rev.* **2000**, *1*, 1–21. [[CrossRef](#)]
11. Linsebigler, A.L.; Lu, G.; Yates, J.T., Jr. Photocatalysis on TiO₂ Surfaces: Principles, Mechanisms and Selected Results. *Chem. Rev.* **1995**, *95*, 735–758. [[CrossRef](#)]

12. Anastasescu, C.; Negrila, C.; Angelescu, D.G.; Atkinson, I.; Anastasescu, M.; Spataru, N.; Zaharescu, M.; Balint, I. Particularities of photocatalysis and formation of reactive oxygen species on insulators and semiconductors: Cases of SiO₂, TiO₂ and their composite SiO₂-TiO₂. *Catal. Sci. Technol.* **2018**, *8*, 5657–5668. [[CrossRef](#)]
13. Fujishima, A.; Zhang, X.; Tryk, D.A. Heterogeneous photocatalysis: From water photolysis to applications in environmental cleanup. *Int. J. Hydrog. Energy* **2007**, *32*, 2664–2672. [[CrossRef](#)]
14. Bumajdad, A.; Madkour, M. Understanding the superior photocatalytic activity of noble metals modified titania under UV and visible light irradiation. *Phys. Chem. Chem. Phys.* **2014**, *16*, 7146–7158. [[CrossRef](#)] [[PubMed](#)]
15. Yang, D.; Lee, S.W. Photocatalytic activity of Ag, Au-Deposited TiO₂ nanoparticles prepared by sonochemical reduction method. *Surface Rev. Lett.* **2010**, *17*, 21–26. [[CrossRef](#)]
16. Tian, Y.; Tatsuma, T. Mechanisms and Applications of Plasmon-Induced Charge Separation at TiO₂ Films Loaded with Gold Nanoparticles. *J. Am. Chem. Soc.* **2005**, *127*, 7632–7637. [[CrossRef](#)]
17. Tanaka, A.; Sakaguchi, S.; Hashimoto, K.; Kominami, H. Preparation of Au/TiO₂ with Metal Cocatalysts Exhibiting Strong Surface Plasmon Resonance Effective for Photoinduced Hydrogen Formation under Irradiation of Visible Light. *ACS Catal.* **2013**, *3*, 79–85. [[CrossRef](#)]
18. Zhai, W.; Xue, S.; Zhu, A.; Luo, Y.; Tian, Y. Plasmon-Driven Selective Oxidation of Aromatic Alcohols to Aldehydes in Water with Recyclable Pt/TiO₂ Nanocomposites. *Chem. Cat. Chem.* **2011**, *3*, 127–130. [[CrossRef](#)]
19. Osterloh, F.E. Nanoscale Effects in Water Splitting Photocatalysis. *Top. Curr. Chem.* **2016**, *371*, 105–142. [[CrossRef](#)]
20. Yoffe, A.D. Semiconductor quantum dots and related systems: Electronic, optical, luminescence and related properties of low dimensional systems. *Adv. Phys.* **2001**, *50*, 1–208. [[CrossRef](#)]
21. Hayyan, M.; Hashim, M.A.; AlNashef, I.M. Superoxide Ion: Generation and Chemical Implications. *Chem. Rev.* **2016**, *116*, 3029–3085. [[CrossRef](#)]
22. Suh, M.; Bagus, P.S.; Pak, S.; Rosynek, M.P.; Lunsford, J.H. Reactions of Hydroxyl Radicals on Titania, Silica, Alumina and Gold Surfaces. *J. Phys. Chem. B* **2000**, *104*, 2736–2742. [[CrossRef](#)]
23. Goto, H.; Hanada, Y.; Ohno, T.; Matsumura, M. Quantitative Analysis of Superoxide Ion and Hydrogen Peroxide Produced from Molecular Oxygen on Photoirradiated TiO₂ Particles. *J. Catal.* **2004**, *225*, 223–229. [[CrossRef](#)]
24. Zhu, S.; Liang, S.; Gu, Q.; Xie, L.; Wang, J.; Ding, Z.; Liu, P. Effect of Au supported TiO₂ with dominant exposed facets on the visible-light photocatalytic activity. *Appl. Catal. B* **2012**, *119*, 146–155. [[CrossRef](#)]
25. Watanabe, K.; Menzel, D.; Nilius, N.; Freund, H.J. Photochemistry on Metal Nanoparticles. *Chem. Rev.* **2006**, *106*, 4301–4320. [[CrossRef](#)]
26. Ueno, K.; Misawa, H. Surface plasmon-enhanced photochemical reactions. *J. Photochem. Photobiol. C Photochem. Rev.* **2013**, *15*, 31–52. [[CrossRef](#)]
27. Nosaka, Y.; Nosaka, A.Y. Generation and Detection of Reactive Oxygen Species in Photocatalysis. *Chem. Rev.* **2017**, *117*, 11302–11336. [[CrossRef](#)]
28. Tung, R.T. Recent Advances in Schottky Barrier Concepts. *Mat. Sci. Eng. R* **2001**, *35*, 1–138. [[CrossRef](#)]
29. Henderson, M.A. A surface science perspective on TiO₂ photocatalysis. *Surface Sci. Rep.* **2011**, *66*, 185–297. [[CrossRef](#)]
30. Fan, H.; Jiang, T.; Li, H.; Wang, D.; Wang, L.; Zhai, J.; He, D.; Wang, P.; Xie, T. Effect of BiVO₄ Crystalline Phases on the Photoinduced Carriers Behavior and Photocatalytic Activity. *J. Phys. Chem. C* **2012**, *116*, 2425–2430. [[CrossRef](#)]
31. Zhang, Y.; Xie, T.; Jiang, T.; Wei, X.; Pang, S.; Wang, X.; Wang, D. Surface photovoltage characterization of a ZnO nanowire array/CdS quantum dot heterogeneous film and its application for photovoltaic devices. *Nanotechnology* **2009**, *20*, 155707. [[CrossRef](#)] [[PubMed](#)]
32. Wu, P.; Wang, J.; Zhao, J.; Guo, L.; Osterloh, F.E. Structure defects in g-C₃N₄ limit visible light driven hydrogen evolution and photovoltage. *J. Mat. Chem. A* **2014**, *2*, 20338–20344. [[CrossRef](#)]
33. Duzhko, V.V.; Timoshenko, V.; Koch, F.; Dittrich, T. Photovoltage in nanocrystalline porous TiO₂. *Phys. Rev. B* **2001**, *64*, 075204. [[CrossRef](#)]
34. Osterloh, F.E.; Holmes, M.A.; Zhao, J.; Chang, L.; Kawula, S.; Roehling, J.D.; Moule, A.J. P3HT:PCBM Bulk-Heterojunctions: Observing Interfacial and Charge Transfer States with Surface Photovoltage Spectroscopy. *J. Phys. Chem. C* **2014**, *118*, 14723–14731. [[CrossRef](#)]
35. Kronik, L.; Shapira, Y. Surface photovoltage spectroscopy of semiconductor structures: At the crossroads of physics, chemistry and electrical engineering. *Surf. Interface Anal.* **2001**, *31*, 954–965. [[CrossRef](#)]
36. Frame, F.A.; Townsend, T.K.; Chamousis, R.L.; Sabio, E.M.; Dittrich, T.; Browning, N.D.; Osterloh, F.E. Photocatalytic Water Oxidation with Nonsensitized IrO₂ Nanocrystals under Visible and UV Light. *J. Am. Chem. Soc.* **2011**, *133*, 7264–7267. [[CrossRef](#)]
37. Shi, F.; Baker, L.R.; Hervier, A.; Somorjai, G.A.; Komvopoulos, K. Tuning the electronic structure of titanium oxide support to enhance the electrochemical activity of platinum nanoparticles. *Nano Lett.* **2013**, *13*, 4469–4474. [[CrossRef](#)]
38. Mirceski, V.; Guziejewski, D.; Bozem, M.; Bogeski, I. Characterizing electrode reactions by multisampling the current in square-wave voltammetry. *Electrochim. Acta* **2016**, *213*, 520–528. [[CrossRef](#)]
39. Sawyer, D.T.; Valentine, J.S. How super is superoxide? *Acc. Chem. Res.* **1981**, *14*, 393–400. [[CrossRef](#)]
40. TBui, D.; Kimura, A.; Ikeda, S.; Matsumura, M. Determination of Oxygen Sources for Oxidation of Benzene on TiO₂ Photocatalysts in Aqueous Solutions Containing Molecular Oxygen. *J. Am. Chem. Soc.* **2010**, *132*, 8453–8458. [[CrossRef](#)]

41. Ilie, A.G.; Scarisoreanu, M.; Dutu, E.; Dumitrache, F.; Banici, A.M.; Fleaca, C.T.; Vasile, E.; Mihailescu, I. Study of phase development and thermal stability in as synthesized TiO₂ nanoparticles by laser pyrolysis: Ethylene uptake and oxygen enrichment. *Appl. Surf. Sci.* **2018**, *427*, 798–806. [[CrossRef](#)]
42. Gupta, N.; Bansal, P.; Pal, B. Metal ion-TiO₂ nanocomposites for the selective photooxidation of benzene to phenol and cycloalkanol to cycloalkanone. *J. Experim. Nanosci.* **2015**, *10*, 148–160. [[CrossRef](#)]
43. State, R.; Scurtu, M.; Miyazaki, A.; Papa, F.; Atkinson, I.; Munteanu, C.; Balint, I. Influence of metal-support interaction on nitrate hydrogenation over Rh and Rh-Cu nanoparticles dispersed on Al₂O₃ and TiO₂ supports. *Arab. J. Chem.* **2017**, *10*, 975–984. [[CrossRef](#)]
44. Preda, S.; Anastasescu, C.; Balint, I.; Umek, P.; Sluban, M.; Negrila, C.C.; Angelescu, D.G.; Bratan, V.; Rusu, A.; Zaharescu, M. Charge separation and ROS generation on tubular sodium titanates exposed to simulated solar light. *Appl. Surf. Sci.* **2019**, *470*, 1053–1063. [[CrossRef](#)]
45. Anastasescu, C.; Zaharescu, M.; Angelescu, D.; Munteanu, C.; Bratan, V.; Spataru, T.; Negrila, C.; Spataru, N.; Balint, I. Defect-related light absorption, photoluminescence and photocatalytic activity of SiO₂ with tubular morphology. *Solar Energ. Mater. Solar Cells* **2017**, *159*, 325–335. [[CrossRef](#)]